Electronic Supplementary Information

Moisture-responsive ultralow-hysteresis polymer ionogels for adhesion-switchable strain sensing

Yichen Zhou,[a] Xing Zhang,[a] Ying Zheng,[b] Junfeng Liu,[b] Yongzhong Bao,[ab] Guorong Shan,[ab] Chengtao Yu*[ab] and Pengju Pan*[ab]

[a] *State Key Laboratory of Chemical Engineering, College of Chemical and Biological Engineering, Zhejiang University, 866 Yuhangtang Road, Hangzhou, 310058, China.*

[b] *Institute of Zhejiang University-Quzhou, 99 Zheda Road, Quzhou, 324000, China.*

* Corresponding author. E-mail: yuchengtao@zju.edu.cn, panpengju@zju.edu.cn.

This PDF file includes:

1. Supplementary results
2. Supplementary movies

1. Supplementary results

Table S1. The references listed in Fig. 2f.

Number	References
S1	*Adv. Mater.* 2020, *32*, 2000600
S2	*Chin. J. Polym. Sci.* 2023, *41*, 1142
S3	*Soft Matter* 2022, *18*, 5934
S4	*ACS Appl. Mater. Interfaces* 2021, *13*, 20653
S5	*ACS Appl. Mater. Interfaces* 2022, *14*, 2029
S6	*ACS Appl. Polym. Mater.* 2023, *5*, 3398
S7	*Eur. Polym. J.* 2021, *144*, 110213
S8	*Chem. Mater.* 2020, *32*, 6384

Table S2 Dissipated energy (W_D) and the work of extension (W_E) for dry PPM75-BIS33 ionogel at different cyclic strains calculated from Fig. 4d.

Strain (mm/mm)	W_D (kJ m^{-3})	W_E (kJ m^{-3})	η_{hys} (%)
1	1.23	12.34	9.98
2	2.88	38.62	7.45
3	4.25	75.26	5.65
4	5.14	122.3	4.20
5	5.62	181.8	3.09
6	7.82	258.4	3.03

Table S3 Dissipated energy (W_D) and the work of extension (W_E) for phase-separated PPM75-BIS33 ionogel at different cyclic strains calculated from Fig. 4e.

Strain (mm/mm)	W_D (kJ m^{-3})	W_E (kJ m^{-3})	η_{hys} (%)
1	1.77	13.17	13.4
2	4.29	40.75	10.5
3	5.75	79.31	7.25
4	8.42	128.0	6.58
5	9.89	187.7	5.27
6	11.49	262.4	4.38
7	13.88	354.3	3.92
8	17.65	465.8	3.79
9	19.61	602.3	3.26

Table S4. The references listed in Fig. 4f.

Number	**References**
S9	*ACS Appl. Mater. Interfaces* 2022, *14*, 2029
S10	*ACS Appl. Mater. Interfaces* 2021, *13*, 20653
S11	*ACS Appl. Mater. Interfaces* 2022, *14*, 32551
S12	*Adv. Funct. Mater.* 2022, *32*, 2204565
S13	*Adv. Mater.* 2021, *33*, 2008849
S14	*Adv. Mater.* 2021, *33*, 2008479
S15	*Adv. Mater.* 2021, *33*, 2105306
S16	*Mater. Horiz.* 2020, *7*, 912
S17	*J. Mater. Chem. C* 2024, *12*, 7351

Table S5. The references listed in Fig. 4g.

Number	References
S18	*ACS Sustain. Chem. Eng.* 2023, *11*, 15031
S19	*Adv. Funct. Mater.* 2023, *33*, 2307367
S20	*Adv. Funct. Mater.* 2022, *32*, 2112293
S21	*Chem. Eng. J.* 2023, *476*, 146840
S22	*Chem. Mater.* 2020, *32*, 6310
S23	*Macromolecules* 2022, *55*, 10950
S24	*Nat. Mater.* 2022, *21*, 359

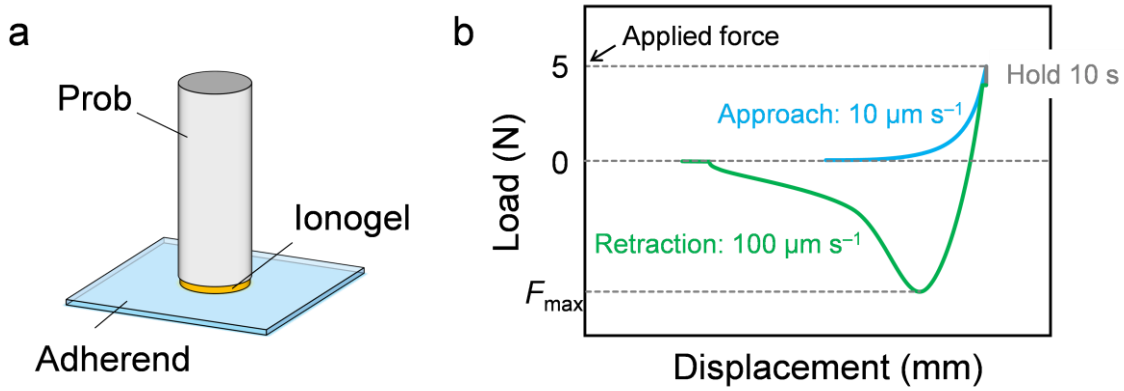

Fig. S1 Tack test for adhesion measurement. Schematic illustration of (a) tack test and (b) load–displacement curve with corresponding parameters. The adhesive strength *G* is determined by the maximum force during the prob retraction divided by contact area.

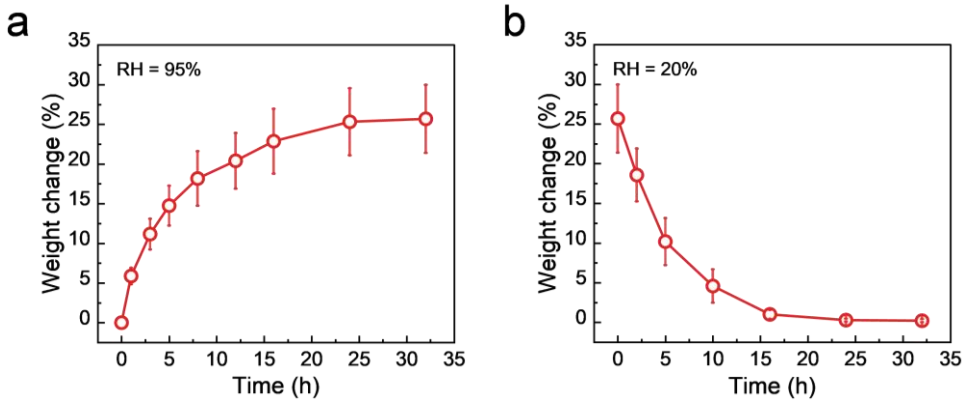

Fig. S2 Determination of processing time under different humidity treatment. Weight changes of the ionogels during (a) hydration process in 95%RH environment and (b) dehydration process in 20%RH environment. Fig. S2 shows that the weight of ionogels varies with the exposure time during the hydration and dehydration process and reaches a plateau after 24 h, indicating that the exchange of moisture between the ionogels and surroundings has reached equilibrium. As such, the humidity processing time of 24 h for both 95%RH and 20%RH environment is chosen for subsequent characterizations and tests.

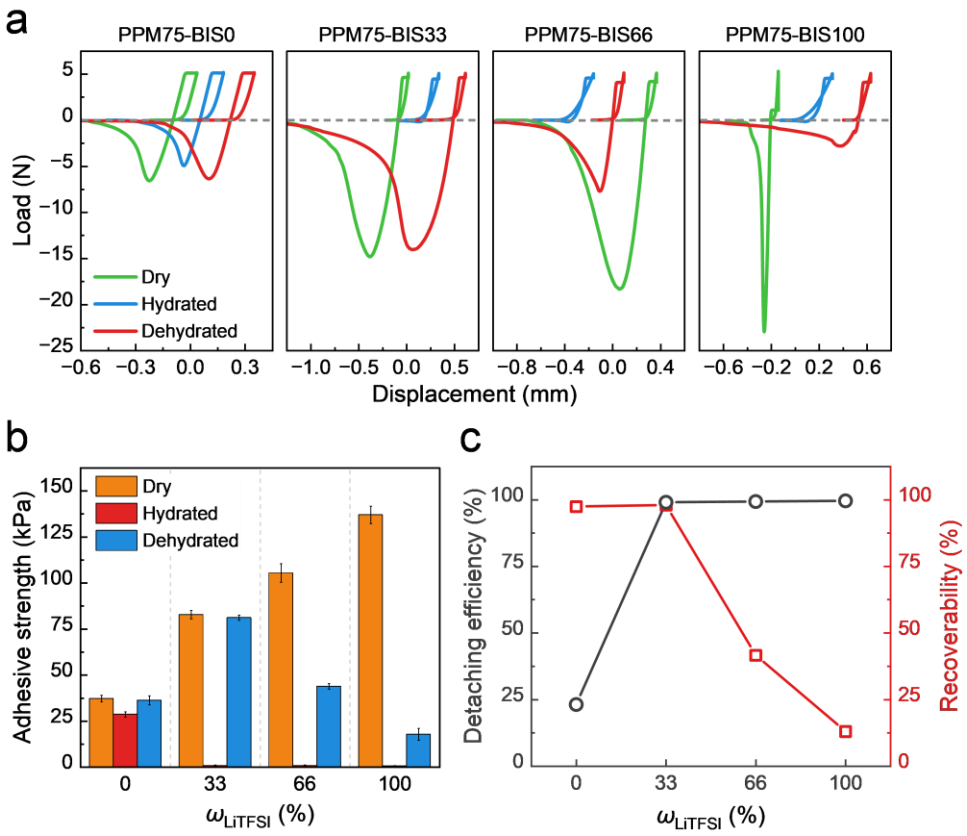

Fig. S3 Effects of ionic solvents composition on the reversible adhesive properties. (a) Load–displacement adhesive curves and (b) the calculated adhesive strength of PPM75-BIS ionogels with different ω_{LiTFSI} after various humidity treatment on the glass substrates. The ionogels equilibrated at 20%RH and 95%RH for 24 h were denoted as the dry ionogels and hydrated ionogels, respectively. Hydrated ionogels placed at 20%RH for 24 h was denoted as the dehydrated ionogels. (c) Comparison of detaching efficiency and adhesive recoverability of PPM75-BIS ionogels with different ω_{LiTFSI}. Fig. S3 shows that the ionogels with higher LiTFSI content (*i.e.*, PPM75-BIS33, PPM75-BIS66, and PPM75-BIS100) exhibit higher adhesive strength at dry state and higher detaching efficiency. However, excessive amount of LiTFSI (*i.e.*, ω_{LiTFSI} = 66% and 100%) leads to the relatively low adhesive recoverability, which could be ascribed to the residual water maintained in the ionogels even at low humidity environment. In summary, PPM75-BIS33 ionogel exhibits overall the highest detaching efficiency and adhesive recoverability, thus the ionogel with ω_{LiTFSI} = 33% was used in further characterizations and application demonstration.

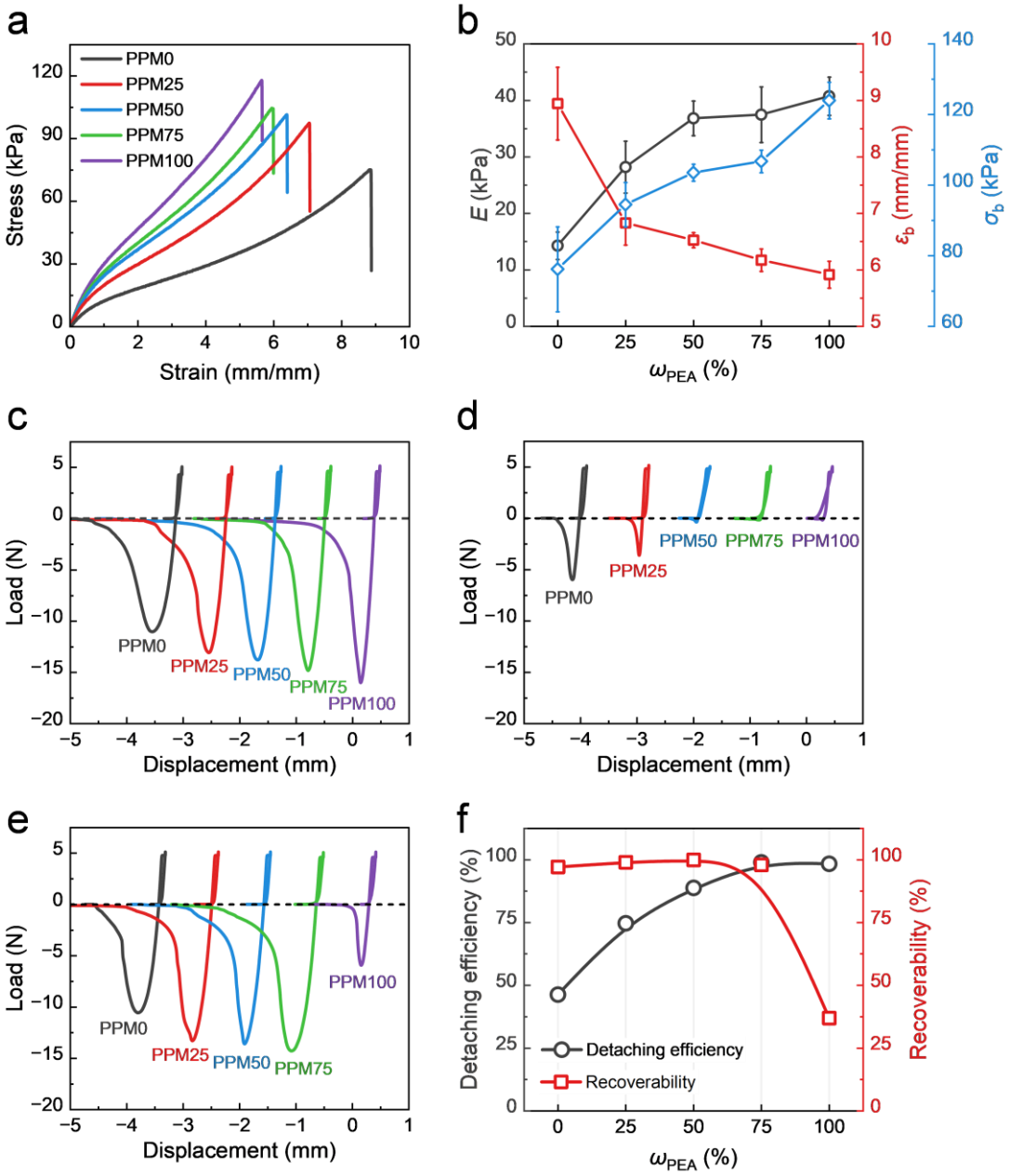

Fig. S4 Effect of monomer composition (ω_{PEA}) on the mechanical and adhesive properties. (a) Uniaxial tensile stress–strain curves and (b) the calculated Young's modulus (E), fracture stress (σ_b), and fracture strain (ε_b) of the PPM-BIS33 ionogels with different monomer compositions. Stretching velocity: 100 mm min^{-1}. (c-e) Load–displacement adhesive curves of (c) dry, (d) hydrated, and (e) dehydrated PPM-BIS33 ionogels with different monomer composition. The hydrated ionogels were dry ionogels placed at 95%RH for 24 h, and the dehydrated ionogels were hydrated ionogels placed at 20%RH for 24 h. (f) Comparison of detaching efficiency and adhesive recoverability of PPM-BIS33 ionogels with different ω_{PEA}. Fig. S4 shows that the ionogels with higher

PEA content (*i.e.*, PPM75-BIS33, and PPM100-BIS33) exhibit higher adhesive strength at dry state and higher detaching efficiency (>98%). However, PPM100-BIS33 ionogels show reduced adhesive recoverability (37%), likely due to the residual water retained in the ionogel even under low-humidity conditions. In summary, PPM75-BIS33 ionogel achieves the best overall switchable adhesive performance. Therefore, the ionogel with ω_{PEA} = 75% was used in further characterizations and application demonstration.

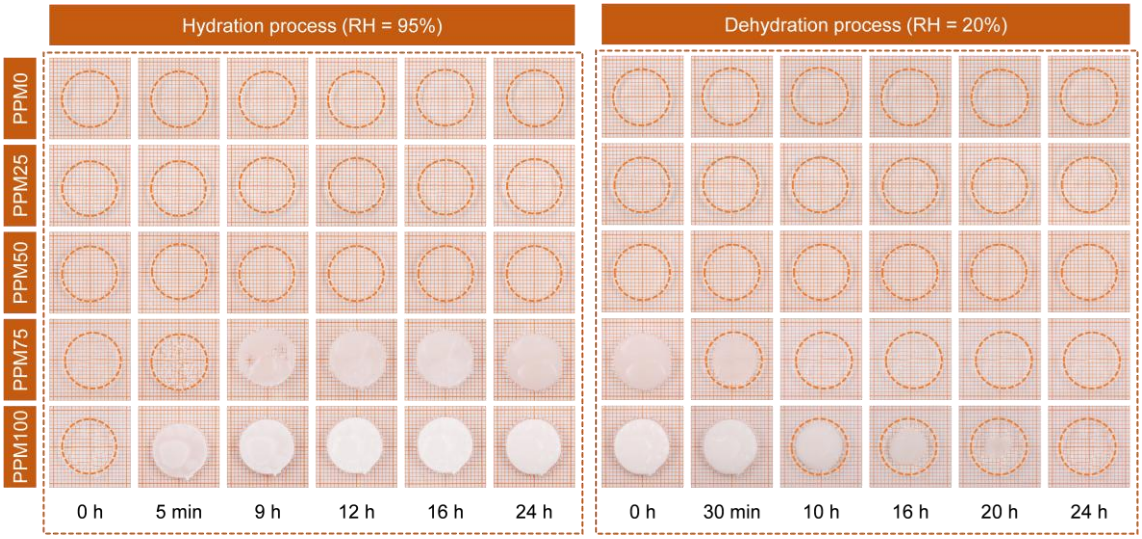

Fig. S5 Effect of monomer composition (ω_{PEA}) on the transparency evolution of PPM-BIS33 during the hydration and dehydration process. The size of each small grid in the photographs is 1 mm.

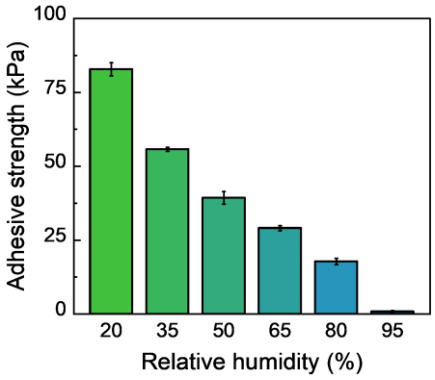

Fig. S6 Effect of environmental humidity on the adhesive strength of PPM75-BIS33.

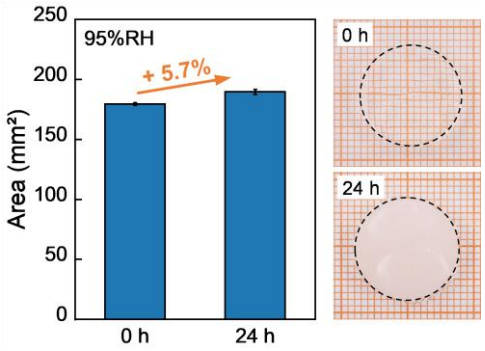

Fig. S7 Size changes of PPM75-BIS33 ionogel before and after the hydration process under 95%RH conditions. As shown in Fig. S7, the area of PPM75-BIS33 ionogel expanded by 5.7% after 24 h of hydration due to water absorption, suggesting that the moisture-mediated phase separation leads to the potential size mismatch at the interface of ionogels and adherends. The size of each small grid in the photographs is 1 mm.

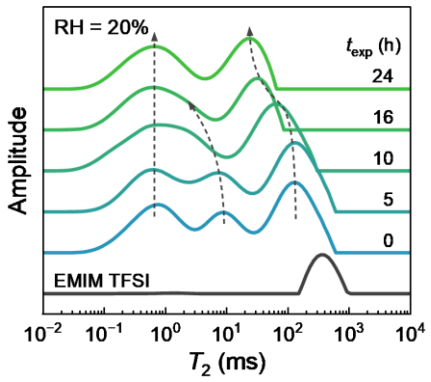

Fig. S8 LF ^{1}H NMR spectra of PPM75-BIS33 and EMIM TFSI during the dehydration process at 20%RH with different t_{exp}.

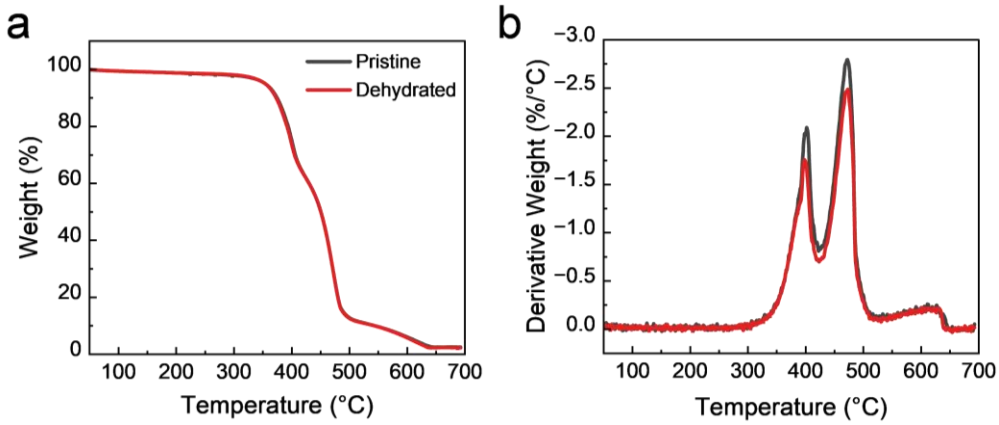

Fig. S9 (a) TGA curves and (b) their derivative curves for the pristine dry and dehydrated PPM75-BIS33 ionogels.

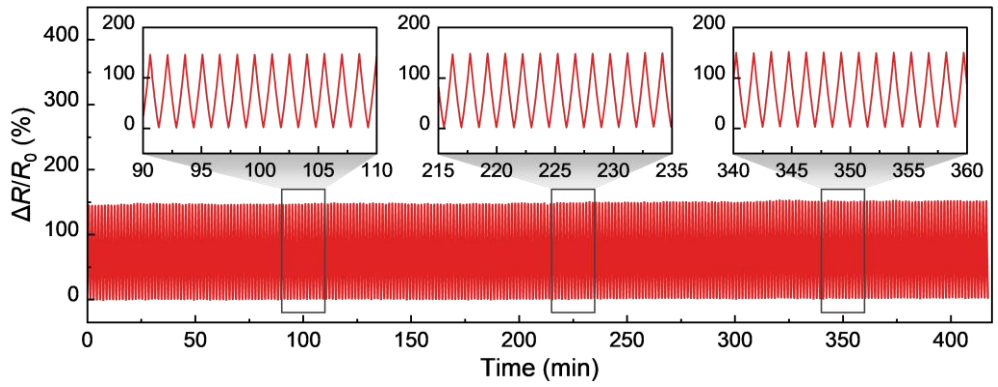

Fig. S10 Cyclic stability test of PPM75-BIS33 under the repetitive loading–unloading strain of 75% for 250 cycles. Insets exhibit the enlarged view of some periods during the whole cyclic test. Stretching velocity: 30 mm min^{-1}.

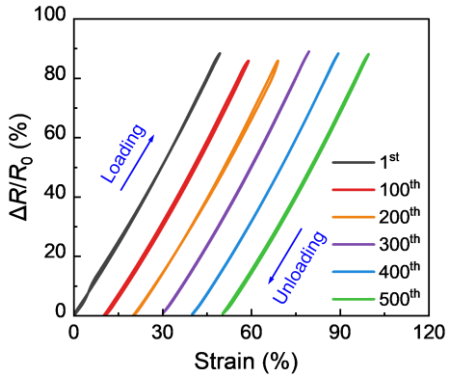

Fig. S11 $\Delta R/R_0$ signals changes with the loading strain during the cyclic stability test shown in Fig. 5e.

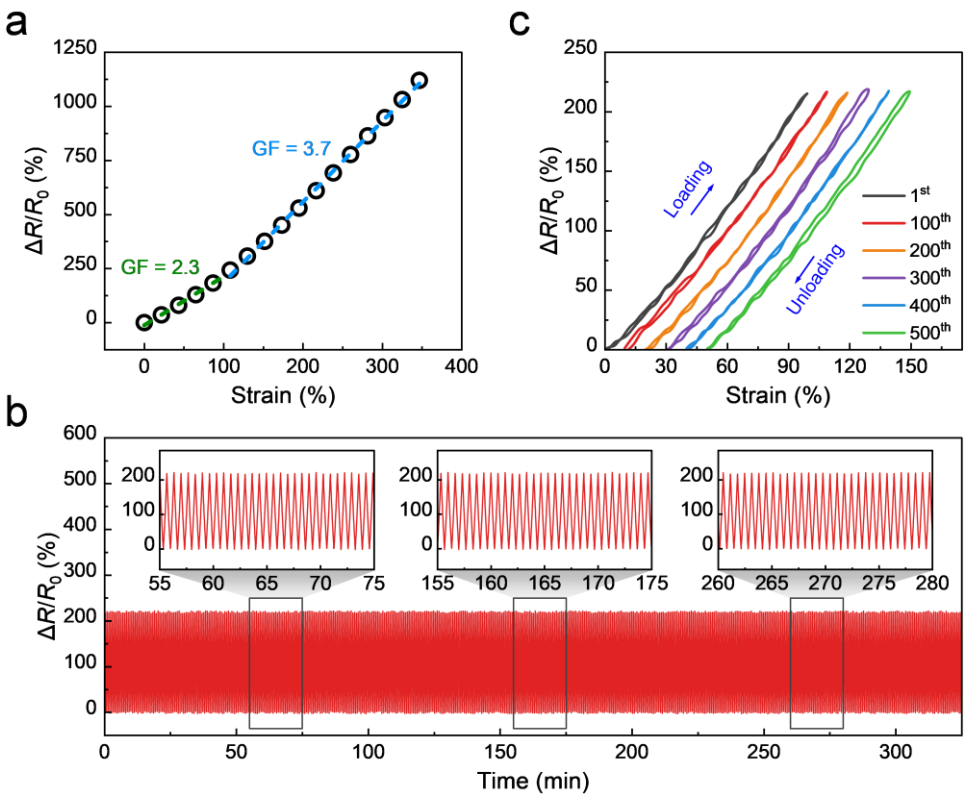

Fig. S12 Strain-sensing performance of phase-separated PPM75-BIS33 ionogel. (a) $\Delta R/R_0$ changes as a function of tensile strain. The black dots denote the experiment data, and the green and blue dashed lines represent the linear fitting curves. (b) Cyclic stability test under the repetitive loading–unloading strain of 100% with the strain rate of 100 mm min^{-1} for 500 cycles. Insets exhibit the enlarged view of some periods during the whole cyclic test. (c) $\Delta R/R_0$ signals changes with the loading strain during the cyclic stability test shown in Fig. S12b. As shown in Fig. S12a, the phase-separated PPM75-BIS33 demonstrates a wide strain sensing window from 0% to 300%. The GF value is calculated as 2.3 below 100% strain and 3.7 in 100%−300% strain range, indicating the good linearity of detection signals. Moreover, the phase-separated ionogel maintains stable output signals during the repeated loading–unloading at 100% strain for 500 cycles in Fig. S12b. During the cyclic test, the phase-separated ionogel demonstrates minimal strain-sensing hysteresis of less than 5%, with the loading and unloading curves mostly overlapped. These results indicate the accurate and stable sensing performance of the phase-separated PPM-BIS ionogels.

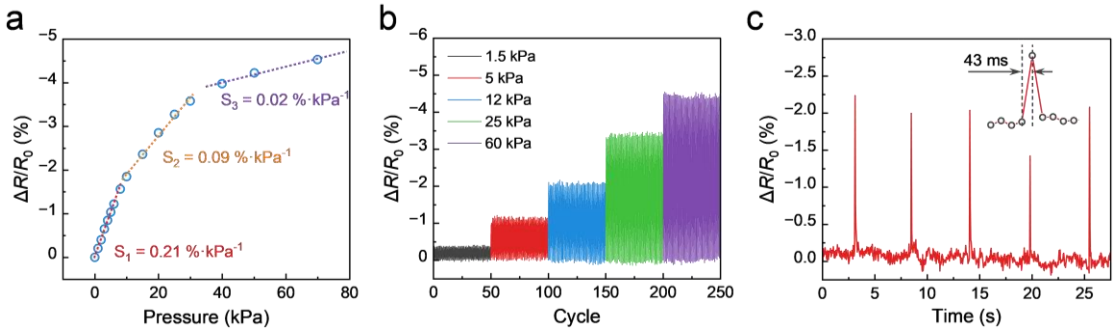

Fig. S13 Pressure sensing performance of moisture-mediated reversible adhesive ionogels. (a) $\Delta R/R_0$ changes as a function of stress. The blue dots denote the experiment data, and the red, orange, and purple dashed lines represent the linear fitting curves. (b) $\Delta R/R_0$ signals measured under different stresses from 1.5 to 60 kPa. (c) Determination of response time and recovery time through rapid continuous tapping on the ionogel.

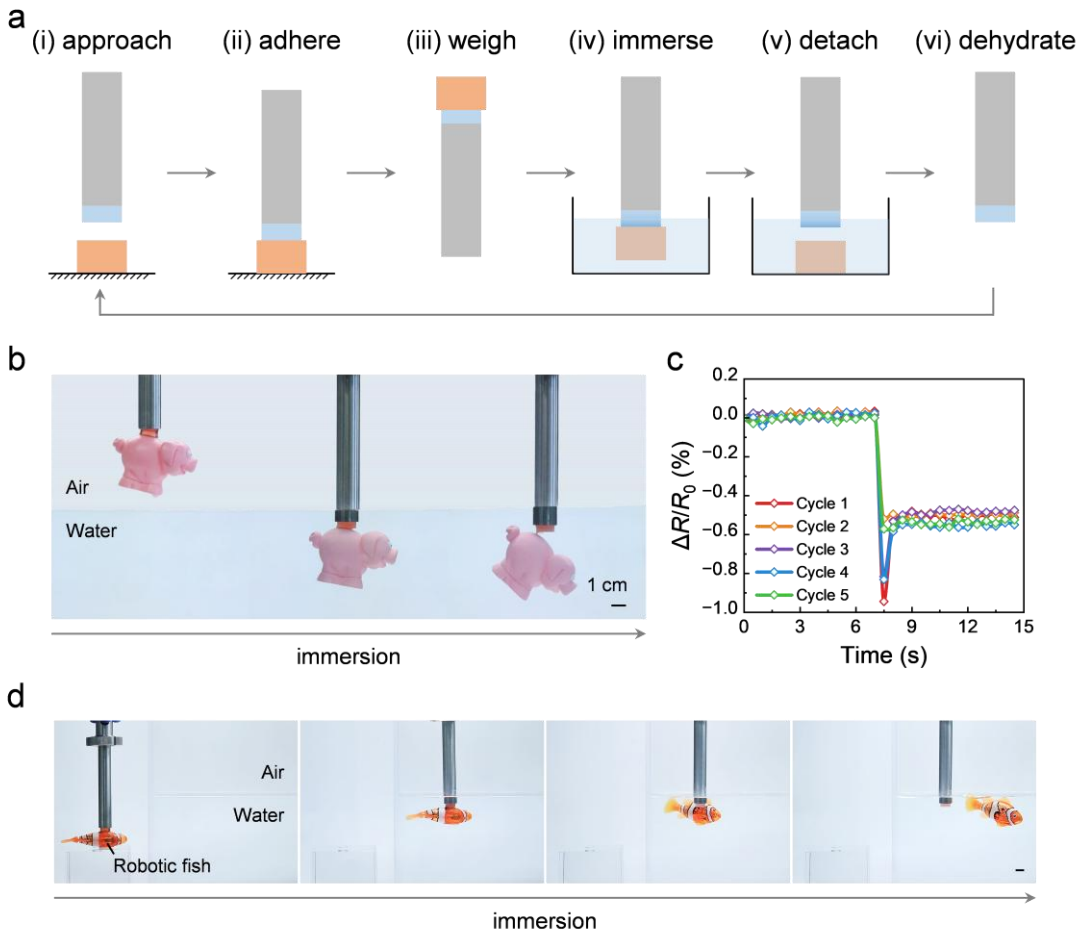

Fig. S14 Demonstration of weigh transfer with the moisture-mediated reversible adhesive ionogels. (a) Schematic illustration of the weigh transfer process that simulated the transfer and weight-capture process in real-life factory production line. The PPM75-BIS33 ionogel was dyed red by Sudan IV for better visualization. Two copper wires were first inserted into both ends of the ionogel to measure the $\Delta R/R_0$ signal changes during the weigh transfer process. The ionogel was attached to one end of a supporting stick using super glue. To accomplish the weigh transfer process, (i) the ionogel approaches the object (ii) until contact and adhesion occur; (iii) the stick, along with the object, is inverted upside down to record the resistance changes induced by the object pressure, thereby determining the object weight; (iv) the stick is then placed upright and the interface between the ionogel and object is immersed in water; (v) after a period of time, the object detaches from the ionogel due to the water-mediated phase separation, leading to the transfer from air to water; (vi) the ionogel is then removed from water to dehydrate and reverse the phase separation for recycling and reuse. (b)

Photographs of transfer process of a pig toy (~47 g) from air to water. (c) $\Delta R/R_0$ signals recorded for weight capture during the cyclic transfer process. The resistance signal changed by about 0.5% with the pressure from the pig toy, which coincides well with the stress–resistance curves shown in Fig. S10. During five transfer cycles, the $\Delta R/R_0$ signal changes remained constant, indicating the good sensing stability of the ionogels. (d) Photographs of transfer process of a robotic fish from air to water. Scale bars: 1 cm.

2. Supplementary movies

Movie S1:

This movie shows that the light-weight sparrow is captured by the adhesive ionogel, and the mechanical clamp is not activated throughout the whole capture process due to the tiny vibration signal from the sparrow. When the water spray is subjected on the ionogel, the sparrow detaches and falls off.

Movie S2:

This movie shows that when the heavy duck is approaching the ionogel, the mechanical clamp is open and the trap is not activated. However, when the duck lands on the ionogel and “flutters” to escape, the mechanical clamp quickly closes and traps the duck. As the duck quiets down, the trap deactivates and release the duck.

Movie S3:

This movie shows that the supporting stick attached with the ionogel approaches a robotic fish and the fish is adhered on the ionogel. Then, the ionogel and fish are transferred and immersed into water. After a period of time, the fish detaches from the ionogel and swims in the water freely.